Imparting Functionality and Enhanced Surface Area to a 2D Electrically Conductive MOF via Macrocyclic Linker

Hoai T. B. Pham,[a,‡] Ji Yong Choi,[a,‡] Shaofeng Huang,[a] Xubo Wang,[a] Adam Claman,[a] Michael Stodolka,[a] Sadegh Yazdi,[b] Sandeep Sharma,[a] Wei Zhang,[a] and Jihye Park[a,*]

[a] Department of Chemistry, University of Colorado Boulder, Boulder, Colorado 80309, United States

[b] Renewable and Sustainable Energy Institute, University of Colorado Boulder, Boulder, Colorado 80309, United States

ABSTRACT: The development of 2D electrically conductive metal-organic frameworks (EC-MOFs) has significantly expanded the scope of MOFs' applications into energy storage, electrocatalysis, and sensors. Despite growing interest in EC-MOFs, they often show low surface area and lack functionality due to the limited ligand motifs available. Herein we present a new EC-MOF using 2,3,8,9,14,15-hexahydroxyltribenzocyclyne (HHTC) linker and Cu nodes, featuring a large surface area. The MOF exhibits an electrical conductivity up to 3.02 x 10^{-3} S/cm and surface area up to 1196 m^2/g, unprecedentedly high for 2D EC-MOFs. We also demonstrate the utilization of alkyne functionality in the framework by post-synthetically hosting hetero-metal ions (e.g., Ni^{2+}, Co^{2+}). Additionally, we investigated particle size tunability, facilitating the study of size-property relationships. We believe that these results not only contribute to expanding the library of EC-MOFs but shed light on the new opportunities to explore electronic applications.

INTRODUCTION

Two-dimensional electrically conductive metal-organic frameworks (2D EC-MOFs) are a newly emerging class of porous electronic materials that inherit most merits from conventional MOFs, such as porosity and tunable chemical functionality, yet show electrical conductivity due to the extended conjugation.[1] The capability to transport electrons within the porous structure has shown their potential in a wide range of applications, including charge-storage materials,[2,3] electrochemical catalysts,[4–6] and chemiresistive sensors.[7] However, to date, 2D EC-MOFs' ligands heavily rely on hexa-substituted benzene[8,9] or hexa-substituted triphenylene,[10,11] which are linked by transition metal ions taking square planar coordination geometry. However, these frameworks impose some unavoidable disadvantages: (i) limited surface area and (ii) lack of functionalizable groups, thus limiting the maximal potential of this emerging class of 2D materials.

To overcome the above challenges, we present a new EC-MOF that consists of 2,3,8,9,14,15-hexahydroxyltribenzocyclyne (HHTC) as the coordinating linker and Cu(II) as the metal node. The HHTC ligand has a fully-conjugated, shape-persistent macrocyclic core with six hydroxyl groups.[12] Topologically, HHTC resembles 2,3,6,7,10,11-hexahydroxytriphenylene (HHTP), an archetype ligand with the same three-fold symmetry, but can, in theory, grant larger surface area due to the bigger size of HHTC and the presence of intrinsic pocket (Figure 1a). Thus, we anticipated the resulting framework would have larger hexagonal pores and potentially functionalizable pockets due to the unique macrocyclic ligand (Figure 1b), which will allow insights into reticular chemistry.

The alkyne moiety in the structure can impart further functionality by post-synthetic metalation. We mapped the electrostatic potentials of HHTC, where the electron-rich *p* orbitals are probed at the ethynyl bonds, potentially good for hosting first-row transition metals, such as nickel and cobalt by providing binding affinity (Figure 1a).[13–15] Hosting hetero-metallic species in the MOF can introduce additional layer of functionalities. For example, nickel can show extremely high sensitivity towards small molecules, such as carbon monoxide[13] and cobalt can work as efficient catalytic sites for electrocatalytic CO_2 reduction.[16]

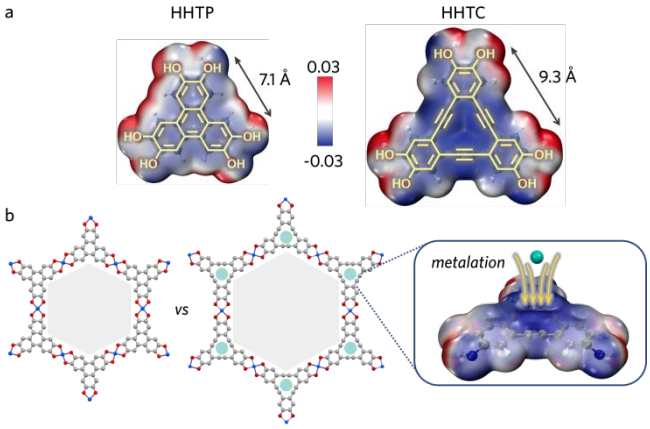

Figure 1. (a) Structures and electrostatic potential maps of HHTP and HHTC ligands. (b) Left: structure of Cu-HHTP with hexagonal pore. Right: structure of Cu-HHTC with hexagonal pore and additional triangular pockets along with proposed inserted metal species in the pocket.

Beyond designing a new ligand motif, precise control over particle size enables tuning the properties of materials, such as surface area, adsorption/desorption kinetics, and diffusion rates.[17] For instance, smaller particles can lead to large surface area, high ratio of exposed active sites, and rapid diffusion of guest molecules into internal pores,[18] which are key parameters for energy-related applications and sensing.

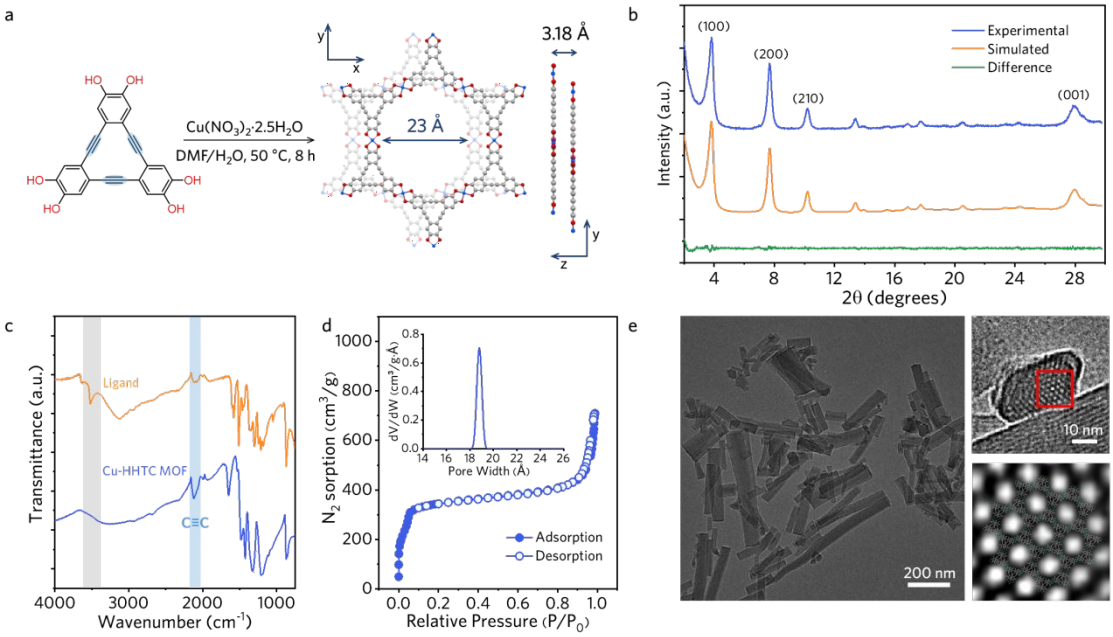

Figure 2. (a) Synthetic scheme of Cu-HHTC. (b) Comparison of experimental and simulated PXRD of Cu-HHTC. (c) FT-IR spectra of the HHTC ligand and Cu-HHTC. The highlight in blue represents the C≡C vibration. (d) N_2 sorption isotherm at 77 K and (inset: pore width). (e) TEM image of Cu-HHTC (left). HR-TEM image along [001] direction (top right). Simulated structure after inverse fast Fourier transform based on the red box (bottom right).

Meanwhile, larger particle sizes can be beneficial to decrease the number of grain boundaries in polycrystalline pellets and improve bulk conductivity. Further, large single crystals can serve as a platform to study intrinsic electronic properties.[11] Although some studies demonstrated the size tunability of conventional MOFs by regulating nucleation and crystal growth stages,[19,20] such a concept remains underexplored in the EC-MOF field because of the fast kinetics of MOF formation. Therefore, we pursued control over particle size, which could provide suitable particle sizes for size-dependent applications and offer insights into the particle size-property relationships within our system.

Herein we present a functionalizable EC-MOF by employing a macrocyclic linker. The $Cu_3(HHTC)_2$, namely Cu-HHTC, exhibited an electrical conductivity up to 3.02 x 10^{-3} S/cm with a large surface area up to 1196 m^2/g, which is considerably higher than those reported for other 2D EC-MOFs, whereas other reported Cu-based HHTP MOFs show surface areas in the range of 306-540 m^2/g.[1,21] We were able to obtain different crystal sizes with varied synthetic parameters and then studied the crystal size effect on surface area and electrical conductivity. Additionally, we demonstrate post-synthetic metalation of Co and Ni into the MOF.

RESULTS AND DISCUSSION

Synthesis and Optimization. While the HHTC linker can be synthesized by cyclooligomerization of ortho-ethynyliodoaryls,[22] bromination/debromination,[23] or spontaneous rearrangements of proximal acetylenes in cyclicdiynes,[24] these synthetic methods yield low with undesirable oligomers, making purification cumbersome. Thus, we adopted advances in reversible alkyne metathesis and successfully synthesized HHTC with a high yield via a highly reactive and selective molybdenum catalyst towards the cyclization, making it practically useful for MOF synthesis (See Supporting Information for synthesis, Figures S1-S5).[25]

Cu-HHTC was synthesized via solvothermal synthesis, where copper(II) nitrate reacted with the HHTC linker. We screened various synthetic parameters, including base, temperature, reaction time, stoichiometry, and solvent compositions to find optimal conditions for Cu-HHTC. We first tested different kind of bases, including sodium acetate, ammonium hydroxide, ethylenediamine, and base-free conditions. The powder X-ray diffraction (PXRD) indicated that the base-free condition affords the framework with higher crystallinity than the reactions with bases (Figure S6). When we investigated the reaction temperatures in the range of 30 °C to 50 °C, the crystallinity exhibited negligible differences, but over 70 °C, it negatively impacted the crystallinity. (Figure S7). Meanwhile, the crystallinity gradually improved as the reaction time extended to 8 hours (Figure S8). We found that the ligand/metal ratios and the co-solvent compositions play a critical role in the Cu-HHTC synthesis. While the ligand to metal ratio of 3:2 is typically used in the literature for 2D EC-MOFs, our optimal ratio was found to be 2:1 (Figure S9). We used a co-solvent system of water and *N,N*-dimethyl formamide (DMF) to optimize the crystal growth. The co-solvent system can moderate the rate of deprotonation, nucleation, and the number of donors, which influence on the dynamics of metal-ligand coordination, thus the crystal growth.[26] We found that 1:1 (v/v) H_2O:DMF substantially improves the crystallinity (Figure S10). Based on the optimized parameters, we obtained highly crystalline Cu-HHTC by using two equivalents of copper nitrate salts to the linker in H_2O:DMF (1:1, v/v) at 50 °C for 8 hours (Figure 2a).

Structure Characterization. The structure of the Cu-HHTC was refined against Pawley fit based on the experimental PXRD (Figure 2b). We compared the experimental PXRD to the simulated AA eclipsed, AA slipped-parallel, and AB staggered models to elucidate its stacking mode. Upon analysis, the AB staggered model was excluded due to its significant difference from the experimental patterns (Figure S11). The simulated AA eclipsed and AA slipped-parallel modes show a notable difference in their layer-to-layer distances, which correspond to a variation at ~28°. The AA slipped-parallel model resolved the peak at 28° that was unindexable with the eclipsed counterpart and gave a better fit to other peaks. Cu-HHTC represents hexagonal unit cell, the space group of *P6/mmm* with the lattice parameters of $a = b = 26.08$ Å and $c = 3.18$ Å (residue $R_w = 3.94\%$) (Table S1). The peak at $2\theta = 3.85°$ assigned to d_{100} of 23 Å, which matches well with the hexagonal pore from the AA slipped-parallel packing.

Fourier transform infrared (FT-IR) spectroscopy of Cu-HHTC shows the disappearance of the O-H stretching vibration of catechol units at 3521 cm^{-1} that was initially present in the HHTC linker, confirming the coordination (Figure 2c). Both ligand and Cu-HHTC spectra display absorption at 2120 cm^{-1}, indicative of C≡C stretching vibration. Thus, it confirms that the alkyne functional group in the linker remains intact after the MOF synthesis. There is a weak broad band at ~3300 cm^{-1} in the Cu-HHTC, which may indicate the presence of water, as was also corroborated by thermogravimetric analysis (TGA) showing a gradual weight loss up to 100 °C (Figure S12).

Then, the porosity and the surface area were investigated by N_2 sorption isotherm at 77 K (Figure 2d). The material shows a remarkably high BET surface area of 1133 m^2/g. This is one of the highest values for copper-based EC-MOFs (Figure S14, Table S2). Zeo++ calculated a large theoretical surface area of 1405 m^2/g, suggesting possible high surface area of our MOF (Table S3). The high surface area could be explained by the excellent crystallinity, the large linker size of HHTC along with the contribution of intrinsic pockets.[27] The non-local density functional theory (NL-DFT) calculated pore width distribution shows the dominant pore size of 19 Å, further supporting the slipped AA stacking mode. X-ray photoelectron spectroscopy (XPS) scan of Cu(2p) suggests the presence of both Cu(I) and Cu(II) centers in the MOF (933.2 eV and 935.1 eV at the 2p3/2 level, respectively),[28] while Cu(II) is dominant with strong characteristic satellite peaks (Figure S15a). The deconvoluted O 1s spectra show two distinguishable binding energies at 531.4 eV and 533.7 eV, which can be ascribed to C=O and C-O, respectively (Figure S15b).[28]

The scanning electron microscopy (SEM) and transmission electron microscopy (TEM) images of Cu-HHTC show rod crystals with an average size of 256 nm (Figure 2e and Figure S16). High-resolution TEM (HR-TEM) analysis along the [001] direction revealed that the pore size of 22 Å with a honeycomb arrangement, which is in good agreement with the proposed slipped AA packing mode.

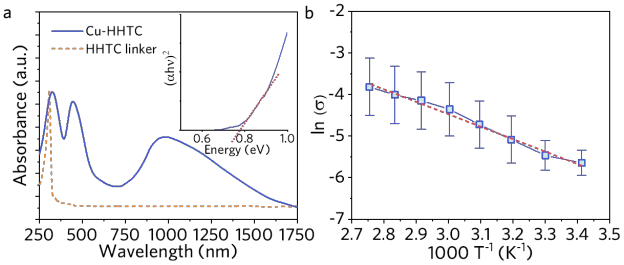

Figure 3. (a) UV-Vis-NIR spectrum of Cu-HHTC MOF and its Tauc-plot (inset). (b) Electrical conductivity of Cu-HHTC under ambient atmosphere.

Electronic Structure Characterization. UV-Vis-NIR spectroscopy of Cu-HHTC exhibits absorption at 1000 nm extending to the near-infrared (NIR) region. This absorption band was not presented in the HHTC linker, indicating a strong d-π conjugation between the metal node and HHTC linker (Figure 3a). The Tauc plot derived from the absorbance spectrum determined the optical bandgap to be 0.78 eV.

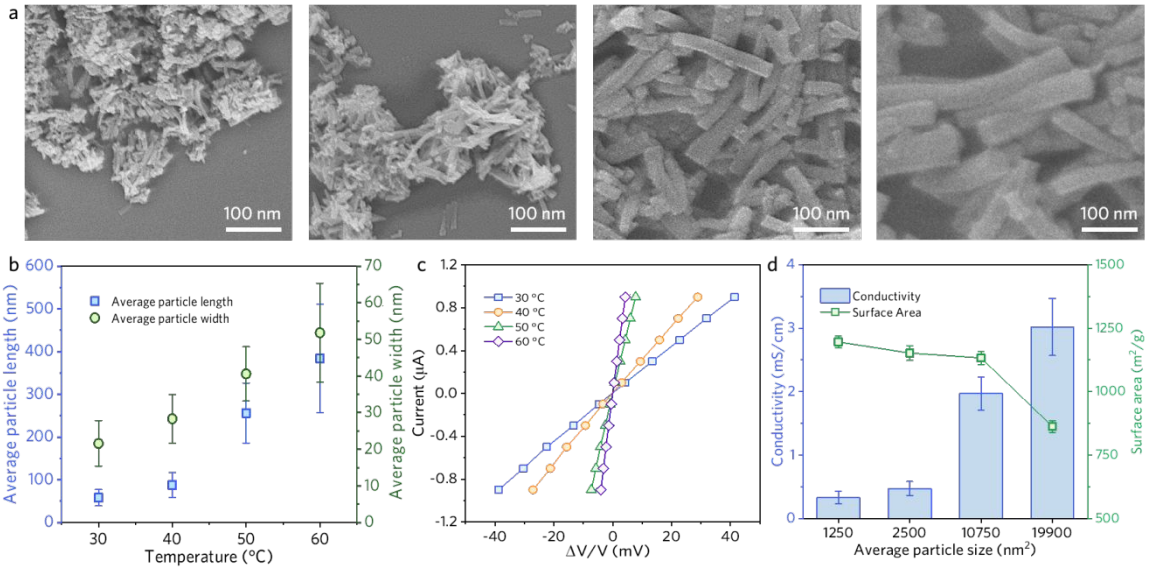

Figure 4. (a) SEM images of Cu-HHTCs, (b) variations of crystal length and width, and (c) I-V curves of Cu-HHTC synthesized with different synthetic temperatures. (d) Electrical conductivity as a function of crystal sizes and their respective surface area.

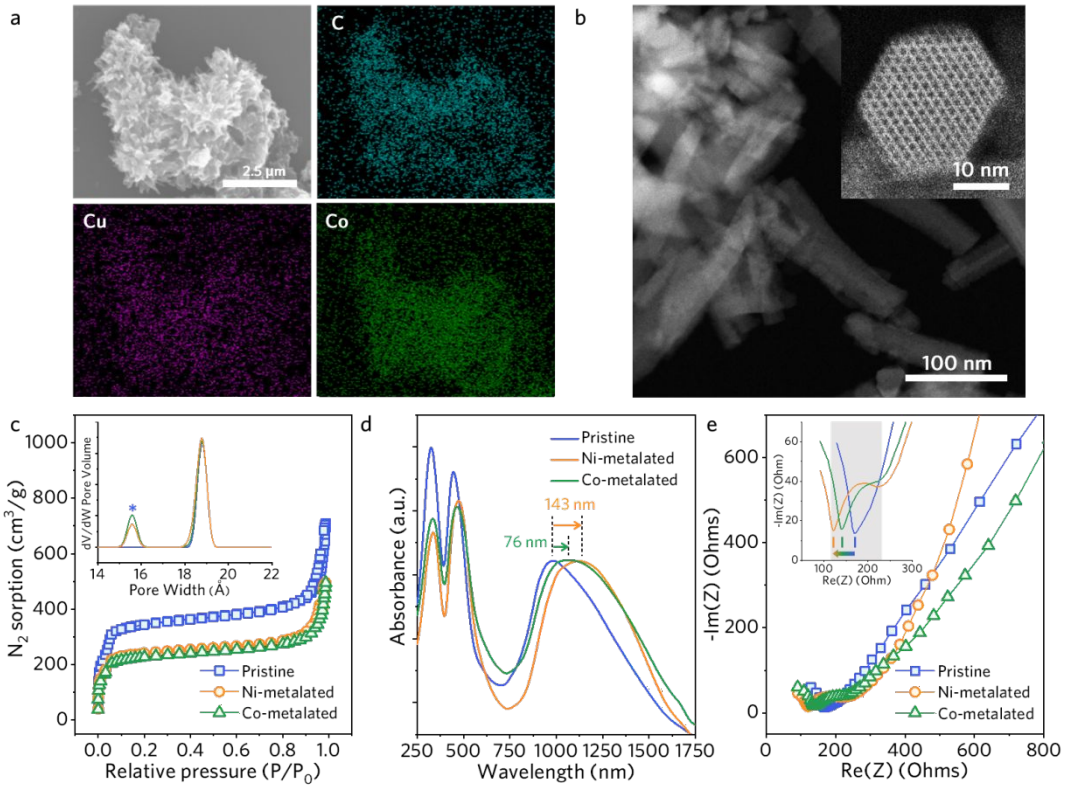

Figure 5. (a) SEM elemental mapping and (b) HAADF-STEM image of Co metalated Cu-HHTC MOF. (c) N_2 sorption isotherm at 77 K and (inset: pore width), (d) UV-Vis-NIR absorption spectra, and (e) electrochemical impedance spectra of pristine and metalated materials.

Next, bulk electrical properties were measured on a pressed pellet *via* the four-point probe method under ambient conditions. Cu-HHTC exhibits an electrical conductivity of 1.97 x 10^{-3} S/cm. Our material shows comparable electrical conductivity to Cu-HHTP, but with a two-fold higher surface area.[29] By fitting the conductivity as a function of temperature (293 K–363 K) to the Arrhenius equation, $\sigma = \sigma_0 \exp(-E_a/k_BT)$, where σ_0 is a pre-factor, E_a is the thermal activation energy, k_B is Boltzmann constant, and T is the absolute temperature, the activation energy was found to be 0.26 eV (Figure 3b). This small activation energy and the optical bandgap explain the semiconducting behaviors of Cu-HHTC.

Particle Size Tunability. To access the controllable particle size of Cu-HHTC, we focused on altering the reaction temperatures which will influence on the nucleation and crystal growth rates.[20,21] When changing the temperature from 30 °C to 60 °C by a 10 °C increment, the average particle size both in length and width increased while retaining the morphology (Figure 4a,b and Figures S17-S19). Herein the particle size was calculated by multiplication of the short side and long side of the particles. Importantly, PXRD data revealed particle size control was achieved without sacrificing crystallinity (Figure S20). The PXRD of smaller particles exhibit a larger full width at half maximum (FWHM), corroborating a similar size trend with the SEM images as a function of temperature (Figure S21). Therefore, by a simple yet effective modification, our Cu-HHTC system provides an opportunity to study size-dependent behaviors on electrical conductivity.

By plotting I-V curves of the materials obtained from different reaction temperatures, we observed changes in conductivity (Figure 4c). The smaller particles with an average size of 1250 nm^2 exhibited a lower conductivity of 3.32 x 10^{-4} S/cm. Whereas, the larger particles of 19900 nm^2 showed an improved conductivity of 3.02 x 10^{-3} S/cm (Figure 4d). The ten-fold improvement in conductivity could be correlated to increasing trend of crystal domain size as particle sizes get larger.[30]

Additionally, we investigated correlation between the particle size and the BET surface area. The samples generated across the different temperatures show similar sorption isotherms and pore size distributions (Figure S22). However, they have slightly different BET surface areas (Figure 4d). For instance, the smallest crystals show the highest surface area of 1196 m^2/g, while the largest sized group shows rather a moderate surface area of 834 m^2/g. The trend found here, regarding particle size dependent surface area, is consistent with other studies on MOFs, where smaller particles allow for a larger exposed surface and a faster diffusion for N_2 sorption.[31–33]

Post-Synthetic Metalation. We further exploited the alkyne chemistry in our system to host first-row transition metals. Encouraged by our Gibbs free energy calculation, we employed Ni and Co to impart additional functionality in the system as a proof-of-concept. According to the calculation results, hosting Ni^{2+} or Co^{2+} in the intrinsic pockets is energetically favored (Table S4).

The post-synthetic metalation was conducted by stirring the pristine Cu-HHTC in the respective metal nitrate solutions in isopropanol (4 equiv. with respect to HHTC) under a nitrogen atmosphere at room temperature for 6 hours. Calculations

revealed that Ni would be in the intrinsic pocket (in-plane) whereas Co would be sandwiched by two pockets (between-planes) (Figure S24). After metalation, simulation shows a noticeable increase of intensity at ~7°, corresponding to d_{110} (13.3 Å) (Figure S23a). Experimental diffractions also confirmed a pronounced intensity at ~7°, corroborating the structure simulation (Figure S23b). FT-IR showed a decrease of absorption at ~2120 cm^{-1} and an increase of absorption at ~1900 cm^{-1} of the C≡C stretching vibration. The shift is because of the electron-donating nature of C≡C towards the inserted ions (Figure S25),[13,14] suggesting the alkyne moieties provided affinity upon metalation. SEM images show the metalated MOFs retained morphology (Figure S26), proving the stability toward the post-synthetic treatments. Energy-dispersive X-ray spectroscopy (EDS) and inductively coupled plasma mass spectroscopy (ICP-MS) confirmed the presence of Ni and Co ions in the materials (Table S5-S7). In particular, the metalated samples show a comparable amount of Cu, compared to the pristine Cu-HHTC, ruling out the possibility of metal exchange. Then, EDS elemental mapping suggests the homogeneous distribution of the inserted metal species (Figure 5a and Figure S27a). High angle annular dark-field scanning transmission electron microscopy (HAADF-STEM) reveals that there were no presence of Co or Ni nanoparticles, ruling out the possibility of self-seeding (Figure 5b and Figure S27b). Furthermore, the high-resolution HAADF-STEM images show hexagonal channels clearly, confirming the structural integrity after the metalation (Figure 5b inset and Figure S26b).

The metalated samples show lower BET surface areas of 796 m^2/g and 753 m^2/g for Ni- and Co-metalated MOFs, respectively. Also, an appearance of smaller pore sizes than the pristine MOF was observed (Figure 5c). We reasoned that the smaller surface areas are attributed to Ni or Co species occupying the pockets and the slight reduction of pore sizes may be due to trapped chemical species within the hexagonal pores.[34] UV-Vis-NIR absorption spectra also indicated a red-shifted peak in the NIR region, implying interaction between the inserted metal species and the MOF (Figure 5d). Cyclic voltammograms of the metalated materials show an additional reduction peak compared to the pristine MOF, which could be attributed to the reduction of the newly inserted ions (Figure S28). Electrochemical impedance spectroscopy (EIS) data indicate smaller resistance built up after metalation (Figure 5e, inset), which is consistent with improved electrical conductivity measured by the four-point probe method (Figure S29). The Ni- and Co-metalated MOFs exhibited an electrical conductivity of 4.51 x 10^{-3} S/cm and 3.57 x 10^{-3} S/cm, respectively. The improved conductivity compared to pristine MOF (1.97 x 10^{-3} S/cm) would be due to intervalence charge transfer between the inserted metal and MOF. Interestingly, the metalated MOFs show an additional semi-circle (gray highlighted in Figure 5e, inset), indicating additional diffusion resistance, which verifies the existence of inserted metals.[35]

Lastly, we carried out the post-synthetic metalation protocol with Cu-HHTP, a structural analog, as a control experiment. After the metalation, Cu-HHTP also maintained the crystallinity as observed in the case of Cu-HHTC (Figure S30). However, the detected amounts of ions were negligible, unlike the Cu-HHTC (Tables S8, S9), further supporting the critical role of the electron-rich alkyne-based pockets in Cu-HHTC, boasting the unique property of Cu-HHTC in metalation.

CONCLUSIONS

In conclusion, we present a new EC-MOF based on a shape-persistent, conjugated macrocyclic linker, HHTC. The MOF exhibits an electrical conductivity of 3.02 x 10^{-3} S/cm and surface area as high as 1196 m^2/g, which is unprecedentedly high for 2D EC-MOFs. In addition, we explored particle size tunability, enabled a study of size-property relationships. Alkyne group in the ligand was then utilized for hosting hetero-metallic species, imparting additional functionality of the framework. We believe that our work not only adds a new ligand motif to the EC-MOFs but provides promising opportunities in electronic applications of EC-MOFs with high surface area and functionality.

EXPERIMENTAL SECTION

Materials and Instrumentations. Chemicals were purchased from Sigma-Aldrich, Oakwood Chemical, or Fisher Scientific, and used without any further purification. Powder X-ray diffraction (PXRD) was taken using a Bruker D8 diffractometer with a Copper beam source (λ = 1.5418 Å) at 40 kV and 40 mA. Scanning electron microscopy (SEM) was carried out on a field emission scanning electron microscope (JEOL JSM-7401F) at 5 kV. SEM energy-dispersive X-ray spectroscopy (EDS) was conducted using Hitachi SU3500. Transmission electron microscopy (TEM) was carried out on Titan Themis GT 300 at 300 kV. Solution-phase UV-Vis-NIR absorption spectra were taken on CARY 5000 UV-Vis spectrophotometer. To prepare the UV-Vis-NIR sample, as-synthesized MOFs were dispersed in isopropyl alcohol. Solid-phase infrared absorption spectra were taken on Cary 630 ATR FT-IR spectrophotometer. Pore size, BET surface area, and N_2 sorption isotherms measurements were carried out with a Micromeritics ASAP 2020 PLUS porosimeter. Nuclear magnetic resonance (NMR) spectroscopy was performed on a Bruker AV-III 300 MHz spectrometer. XPS was measured by using a K-alpha spectrometer with an Al Kα X-ray source. Thermal gravimetric analysis was performed on a TGA 550 from TA Instruments under N_2 flow at 25 to 500 °C. The composition ratio was measured using iCAP 6300 Duo inductively coupled plasma-atomic emission spectroscopy (ICP-AES). Electrical conductivity was measured with a Keithley SCS-4200 parameter analyzer using the four-point probe method. Pressed pellets were prepared with approximately 5 mg of material in a 5 mm diameter circular dye under 1.5 Tons of pressure. Cyclic voltammetry and electrochemical impedance spectroscopy measurements were conducted in a 0.1 M tetrabutylammonium hexafluorophosphate electrolyte solution in acetonitrile using Biologic VSP 300 Biologic Potentiostat with drop-casted MOF particles on a 5 mm diameter glassy carbon electrode as the working electrode and Ag/Ag^+ as the reference electrode.

Synthesis of Cu-HHTC. HHTC ligand (10 mg, 0.025 mmol) was added to a 20-mL vial charged with a stir bar, followed by 5 mL degassed DMF. Then, $Cu(NO_3)_2{\cdot}2.5H_2O$ (11.7 mg, 0.05 mmol) was dissolved in 5 mL degassed H_2O, and the solution was transferred to the reaction vial. The solution was stirred at

50 °C, 100 rpm, for 8 hours. After 8 hours, the reaction was cooled to room temperature. The black solid product was isolated by centrifugation, washed with DMF (2 x 10 mL), followed by acetone (2 x 10 mL). The product was then dried in a vacuum oven (20 mTorr) at 70 °C for 1 hour.

Synthesis of Cu-HHTC with different particle sizes. Cu-HHTC was synthesized using the same protocol above except within different temperatures from 30 °C to 40 °C, 50 °C, and 60 °C.

Post-synthetic metalation of Cu-HHTC. Pristine Cu-HHTC (25 mg, 0.025 mmol ligand pocket) was added to a 20 mL vial charged with a stir bar. Then, 5 mL of 20 mM (4 equiv.) $Ni(NO_3)_2{\cdot}6H_2O$ or $Co(NO_3)_2{\cdot}6H_2O$ in isopropanol was added to the vial. The mixture was stirred at room temperature for 6 hours under N_2 atmosphere. The mixture was centrifuged to isolate the solid, which was then washed with acetone (10 mL) and dried in a vacuum oven (20 mTorr) at 70 °C for 1 hour.

ASSOCIATED CONTENT

Supporting Information. This material is available free of charge via the Internet at http://pubs.acs.org.
Synthesis of HHTC, synthetic optimization of Cu-HHTC, computational methods, structural characterizations with PXRD, N_2 isotherm, SEM, TEM, and XPS

AUTHOR INFORMATION

Corresponding Author

Jihye Park – *Department of Chemistry, University of Colorado Boulder, Boulder, Colorado 80309, United States*; Email: Jihye.Park@colorado.edu

Authors

Hoai T. B. Pham – *Department of Chemistry, University of Colorado Boulder, Boulder, Colorado 80309, United States*
Ji Yong Choi – *Department of Chemistry, University of Colorado Boulder, Boulder, Colorado 80309, United States*
Shaofeng Huang – *Department of Chemistry, University of Colorado Boulder, Boulder, Colorado 80309, United States*
Xubo Wang – *Department of Chemistry, University of Colorado Boulder, Boulder, Colorado 80309, United States*
Adam Claman – *Department of Chemistry, University of Colorado Boulder, Boulder, Colorado 80309, United States*
Michael Stodolka – *Department of Chemistry, University of Colorado Boulder, Boulder, Colorado 80309, United States*
Sadegh Yazdi –*Renewable and Sustainable Energy Institute, University of Colorado Boulder, Boulder, Colorado 80309, United States*
Sandeep Sharma – *Department of Chemistry, University of Colorado Boulder, Boulder, Colorado 80309, United States*
Wei Zhang – *Department of Chemistry, University of Colorado Boulder, Boulder, Colorado 80309, United States*

Author Contributions

‡These authors contributed equally to this work. All authors have given approval to the final version of the manuscript.

Notes

The authors declare no competing financial interest

ACKNOWLEDGMENT

J.P. acknowledges the start-up funds from the University of Colorado Boulder. J.Y.C. acknowledges support by the Postdoctoral Fellowship from the National Research Foundation of Korea under grant no. NRF-2021R1A6A3A14044659. W.Z. thanks the support from National Science Foundation (CHE-2108197). S.Y. thanks the support from the Facility for Electron Microscopy of Materials at the University of Colorado at Boulder (CU FEMM, RRID: SCR_019306).

REFERENCES

(1) Xie, L. S.; Skorupskii, G.; Dincă, M. Electrically Conductive Metal–Organic Frameworks. *Chem. Rev.* **2020**, *120* (16), 8536–8580. https://doi.org/10.1021/acs.chemrev.9b00766.

(2) Banda, H.; Dou, J.-H.; Chen, T.; Libretto, N. J.; Chaudhary, M.; Bernard, G. M.; Miller, J. T.; Michaelis, V. K.; Dincă, M. High-Capacitance Pseudocapacitors from Li^+ Ion Intercalation in Nonporous, Electrically Conductive 2D Coordination Polymers. *J. Am. Chem. Soc.* **2021**, *143* (5), 2285–2292.

(3) Nam, K. W.; Park, S. S.; dos Reis, R.; Dravid, V. P.; Kim, H.; Mirkin, C. A.; Stoddart, J. F. Conductive 2D Metal-Organic Framework for High-Performance Cathodes in Aqueous Rechargeable Zinc Batteries. *Nat. Commun.* **2019**, *10* (1), 4948.

(4) Miner, E. M.; Fukushima, T.; Sheberla, D.; Sun, L.; Surendranath, Y.; Dincă, M. Electrochemical Oxygen Reduction Catalysed by Ni_3(Hexaiminotriphenylene)$_2$. *Nat. Commun.* **2016**, *7* (1), 10942.

(5) Clough, A. J.; Yoo, J. W.; Mecklenburg, M. H.; Marinescu, S. C. Two-Dimensional Metal–Organic Surfaces for Efficient Hydrogen Evolution from Water. *J. Am. Chem. Soc.* **2015**, *137* (1), 118–121.

(6) Park, J.; Chen, Z.; Flores, R. A.; Wallnerström, G.; Kulkarni, A.; Nørskov, J. K.; Jaramillo, T. F.; Bao, Z. Two-Dimensional Conductive Ni-HAB as a Catalyst for the Electrochemical Oxygen Reduction Reaction. *ACS Appl. Mater. Interfaces* **2020**, *12* (35), 39074–39081.

(7) Meng, Z.; Aykanat, A.; Mirica, K. A. Welding Metallophthalocyanines into Bimetallic Molecular Meshes for Ultrasensitive, Low-Power Chemiresistive Detection of Gases. *J. Am. Chem. Soc.* **2019**, *141* (5), 2046–2053.

(8) Feng, D.; Lei, T.; Lukatskaya, M. R.; Park, J.; Huang, Z.; Lee, M.; Shaw, L.; Chen, S.; Yakovenko, A. A.; Kulkarni, A.; Xiao, J.; Fredrickson, K.; Tok, J. B.; Zou, X.; Cui, Y.; Bao, Z. Robust and Conductive Two-Dimensional Metal−organic Frameworks with Exceptionally High Volumetric and Areal Capacitance. *Nat. Energy* **2018**, *3* (1), 30–36.

(9) Park, J.; Hinckley, A. C.; Huang, Z.; Feng, D.; Yakovenko, A. A.; Lee, M.; Chen, S.; Zou, X.; Bao, Z. Synthetic Routes for a 2D Semiconductive Copper Hexahydroxybenzene Metal–Organic Framework. *J. Am. Chem. Soc.* **2018**, *140* (44), 14533–14537.

(10) Hmadeh, M.; Lu, Z.; Liu, Z.; Gándara, F.; Furukawa, H.; Wan, S.; Augustyn, V.; Chang, R.; Liao, L.; Zhou, F.; Perre, E.; Ozolins, V.; Suenaga, K.; Duan, X.; Dunn, B.; Yamamto, Y.; Terasaki, O.; Yaghi, O. M. New Porous Crystals of Extended Metal-Catecholates. *Chem. Mater.* **2012**, *24* (18), 3511–3513.

(11) Day, R. W.; Bediako, D. K.; Rezaee, M.; Parent, L. R.; Skorupskii, G.; Arguilla, M. Q.; Hendon, C. H.; Stassen, I.; Gianneschi, N. C.; Kim, P.; Dincă, M. Single Crystals of

Electrically Conductive Two-Dimensional Metal–Organic Frameworks: Structural and Electrical Transport Properties. *ACS Cent. Sci.* **2019**, *5* (12), 1959–1964.

(12) Youngs, W. J.; Tessier, C. A.; Bradshaw, J. D. *Ortho* -Arene Cyclynes, Related Heterocyclynes, and Their Metal Chemistry. *Chem. Rev.* **1999**, *99* (11), 3153–3180.

(13) Ferrara, J. D.; Tanaka, A. A.; Fierro, C.; Tessier-Youngs, C. A.; Youngs, W. J. Synthesis and Structural and Theoretical Characterization of a Nickel(0) Complex of Tribenzocyclyne (TBC) and the Preparation of a Novel Organometallic Conductor. *Organometallics* **1989**, *8* (9), 2089–2098.

(14) Djebli, A.; Ferrara, J. D.; Tessier-Youngs, C.; Youngs, W. J. The Synthesis and Structural Characterization of a Novel Tetracobalt Cluster of 5,6,11 ,12,17,18-Hexadehydrotribenzo[a,e,i]-Cyclododecine. *J Chem Soc Chem Commun* **1988**, 548–549.

(15) Ferrara, J. D.; Tessier-Youngs, C.; Youngs, W. J. Synthesis and Characterization of the First Transition Metal Complex of 1,2:5,6:9,10-Tribenzocyclododeca-1,5,9-Triene-3,7,11-Triyne. *J. Am. Chem. Soc.* **1985**, *107* (23), 6719–6721.

(16) Marianov, A. N.; Kochubei, A. S.; Roman, T.; Conquest, O. J.; Stampfl, C.; Jiang, Y. Resolving Deactivation Pathways of Co Porphyrin-Based Electrocatalysts for CO_2 Reduction in Aqueous Medium. *ACS Catal.* **2021**, *11* (6), 3715–3729.

(17) Usman, K. A. S.; Maina, J. W.; Seyedin, S.; Conato, M. T.; Payawan, L. M.; Dumée, L. F.; Razal, J. M. Downsizing Metal–Organic Frameworks by Bottom-up and Top-down Methods. *NPG Asia Mater.* **2020**, *12* (1), 58.

(18) Zavyalova, A. G.; Kladko, D. V.; Chernyshov, I. Yu.; Vinogradov, V. V. Large MOFs: Synthesis Strategies and Applications Where Size Matters. *J. Mater. Chem. A* **2021**, *9* (45), 25258–25271.

(19) Horcajada, P.; Gref, R.; Baati, T.; Allan, P. K.; Maurin, G.; Couvreur, P.; Férey, G.; Morris, R. E.; Serre, C. Metal–Organic Frameworks in Biomedicine. *Chem. Rev.* **2012**, *112* (2), 1232–1268.

(20) He, C.; Liu, D.; Lin, W. Nanomedicine Applications of Hybrid Nanomaterials Built from Metal–Ligand Coordination Bonds: Nanoscale Metal–Organic Frameworks and Nanoscale Coordination Polymers. *Chem. Rev.* **2015**, *115* (19), 11079–11108.

(21) Li, W.-H.; Ding, K.; Tian, H.-R.; Yao, M.-S.; Nath, B.; Deng, W.-H.; Wang, Y.; Xu, G. Conductive Metal–Organic Framework Nanowire Array Electrodes for High-Performance Solid-State Supercapacitors. *Adv. Funct. Mater.* **2017**, *27* (27), 1702067.

(22) Solooki, D.; Ferrara, J. D.; Malaba, D.; Bradshaw, J. D.; Tessier, C. A.; Youngs, W. J.; John, J. A.; Tour, J. M. Tribenzocyclyne (TBC) and Tetrabenzocyclyne (QBC). In *Inorganic Syntheses*; John Wiley & Sons, Ltd, 1996; pp 122–128.

(23) Untch, K. G.; Wysocki, D. C. Cyclododecatrienetriyne. *J. Am. Chem. Soc.* **1966**, *88* (11), 2608–2610.

(24) van Roosmalen, J. H.; Jones, E.; Kevelam, H. J. A Novel Polycyclic Triamine Derivative of Tridehydro[12]Annulene and Its Nitroxides. *Tetrahedron Lett.* **1972**, *13* (19), 1865–1868.

(25) Ge, Y.; Huang, S.; Hu, Y.; Zhang, L.; He, L.; Krajewski, S.; Ortiz, M.; Jin, Y.; Zhang, W. Highly Active Alkyne Metathesis Catalysts Operating under Open Air Condition. *Nat. Commun.* **2021**, *12* (1), 1136.

(26) Chen, T.; Dou, J.-H.; Yang, L.; Sun, C.; Libretto, N. J.; Skorupskii, G.; Miller, J. T.; Dincă, M. Continuous Electrical Conductivity Variation in M_3(Hexaiminotriphenylene)$_2$ (M = Co, Ni, Cu) MOF Allogs. *J. Am. Chem. Soc.* **2020**, *142* (28), 12367–12373.

(27) Dou, J.-H.; Arguilla, M. Q.; Luo, Y.; Li, J.; Zhang, W.; Sun, L.; Mancuso, J. L.; Yang, L.; Chen, T.; Parent, L. R.; Skorupskii, G.; Libretto, N. J.; Sun, C.; Yang, M. C.; Dip, P. V.; Brignole, E. J.; Miller, J. T.; Kong, J.; Hendon, C. H.; Sun, J.; Dincă, M. Atomically Precise Single-Crystal Structures of Electrically Conducting 2D Metal–Organic Frameworks. *Nat. Mater.* **2021**, *20* (2), 222–228.

(28) Mendecki, L.; Mirica, K. A. Conductive Metal–Organic Frameworks as Ion-to-Electron Transducers in Potentiometric Sensors. *ACS Appl. Mater. Interfaces* **2018**, *10* (22), 19248–19257.

(29) Smith, M. K.; Jensen, K. E.; Pivak, P. A.; Mirica, K. A. Direct Self-Assembly of Conductive Nanorods of Metal–Organic Frameworks into Chemiresistive Devices on Shrinkable Polymer Films. *Chem. Mater.* **2016**, *28* (15), 5264–5268.

(30) Park, J.; Lee, M.; Feng, D.; Huang, Z.; Hinckley, A. C.; Yakovenko, A.; Zou, X.; Cui, Y.; Bao, Z. Stabilization of Hexaaminobenzene in a 2D Conductive Metal–Organic Framework for High Power Sodium Storage. *J. Am. Chem. Soc.* **2018**, *140* (32), 10315–10323.

(31) Xia, W.; Zhu, J.; Guo, W.; An, L.; Xia, D.; Zou, R. Well-Defined Carbon Polyhedrons Prepared from Nano Metal–Organic Frameworks for Oxygen Reduction. *J Mater Chem A* **2014**, *2* (30), 11606–11613.

(32) Jung, D.-W.; Yang, D.-A.; Kim, J.; Kim, J.; Ahn, W.-S. Facile Synthesis of MOF-177 by a Sonochemical Method Using 1-Methyl-2-Pyrrolidinone as a Solvent. *Dalton Trans.* **2010**, *39* (11), 2883.

(33) Xiang, Z.; Cao, D.; Shao, X.; Wang, W.; Zhang, J.; Wu, W. Facile Preparation of High-Capacity Hydrogen Storage Metal-Organic Frameworks: A Combination of Microwave-Assisted Solvothermal Synthesis and Supercritical Activation. *Chem. Eng. Sci.* **2010**, *65*, 3140–3146.

(34) Baldwin, L. A.; Crowe, J. W.; Pyles, D. A.; McGrier, P. L. Metalation of a Mesoporous Three-Dimensional Covalent Organic Framework. *J. Am. Chem. Soc.* **2016**, *138* (46), 15134–15137.

(35) Mei, B.-A.; Munteshari, O.; Lau, J.; Dunn, B.; Pilon, L. Physical Interpretations of Nyquist Plots for EDLC Electrodes and Devices. *J. Phys. Chem. C* **2018**, *122* (1), 194–206.

For Table of Contents Only